

Central Lancashire Online Knowledge (CLoK)

Title	Lubricated loaded tooth contact analysis and non-newtonian thermoelastohydrodynamics of high-performance spur gear transmission systems
Type	Article
URL	https://clock.uclan.ac.uk/32078/
DOI	https://doi.org/10.3390/lubricants8020020
Date	2020
Citation	Sivayogan, Gajarajan, Rahmani, Ramin and Rahnejat, Homer (2020) Lubricated loaded tooth contact analysis and non-newtonian thermoelastohydrodynamics of high-performance spur gear transmission systems. <i>Lubricants</i> , 8 (2). p. 20. ISSN 2075-4442
Creators	Sivayogan, Gajarajan, Rahmani, Ramin and Rahnejat, Homer

It is advisable to refer to the publisher's version if you intend to cite from the work.
<https://doi.org/10.3390/lubricants8020020>

For information about Research at UCLan please go to <http://www.uclan.ac.uk/research/>

All outputs in CLoK are protected by Intellectual Property Rights law, including Copyright law. Copyright, IPR and Moral Rights for the works on this site are retained by the individual authors and/or other copyright owners. Terms and conditions for use of this material are defined in the <http://clock.uclan.ac.uk/policies/>



Article

Lubricated Loaded Tooth Contact Analysis and Non-Newtonian Thermoelastohydrodynamics of High-Performance Spur Gear Transmission Systems

Gajarajan Sivayogan ^{*}, Ramin Rahmani and Homer Rahnejat

Wolfson School of Mechanical, Electrical and Manufacturing Engineering, Loughborough University, Leicestershire LE11 3TU, UK; r.rahmani@lboro.ac.uk (R.R.); H.Rahnejat@lboro.ac.uk (H.R.)

* Correspondence: g.sivayogan@lboro.ac.uk

Received: 19 December 2019; Accepted: 11 February 2020; Published: 14 February 2020



Abstract: Energy efficiency and functional reliability are the two key requirements in the design of high-performance transmissions. Therefore, a representative analysis replicating real operating conditions is essential. This paper presents the thermoelastohydrodynamic lubrication (TEHL) of meshing spur gear teeth of high-performance racing transmission systems, where high generated contact pressures and lubricant shear lead to non-Newtonian traction. The determination of the input contact geometry of meshing pairs as well as contact kinematics are essential steps for representative TEHL. These are incorporated in the current analysis through the use of Lubricated Loaded Tooth Contact Analysis (LLTCA), which is far more realistic than the traditional Tooth Contact Analysis (TCA). In addition, the effects of lubricant and flash surface temperature rise of contacting pairs, leading to the thermal thinning of lubricant, are taken into account using a thermal network model. Furthermore, high-speed contact kinematics lead to shear thinning of the lubricant and reduce the film thickness under non-Newtonian traction. This comprehensive approach based on established TEHL analysis, particularly including the effect of LLTCA on the TEHL of spur gears, has not hitherto been reported in literature.

Keywords: high performance transmissions; spur gears; tooth contact analysis; thermoelastohydrodynamics; friction; transmission efficiency

1. Introduction

Spur gears are used in a multitude of engineering applications, including but not limited to automotive transmissions. There is a growing volume of legislation, stringent directives, and regulated targets to reduce harmful emissions from all machinery, particularly from road transport, thus requiring ever-improved energy-efficient transmissions. It is also important to improve noise, vibration, and harshness (NVH) refinement of all gearing systems, as this is another customer-demanded attribute. Additionally, the structural integrity and durability of all mechanical components such as gearing and bearings is of primary concern, particularly with the ever-harsher operating conditions (increased loading, faster contact kinematics, and elevated temperatures). It has been shown that operating conditions for transmissions affect their energy consumption and NVH performance, which are interlinked and often require contradictory methods of palliation [1]. The current investigation focuses on the transmission efficiency and structural integrity of spur gears of high-performance vehicles.

It is now well-established that some degree of traction is needed to transmit power through gear interactions. However, beyond a certain limit, excess traction can lead to power loss throughout a typical meshing cycle [2–4]. Therefore, it is important to develop techniques to predict the generated friction, thus accurately assessing the power losses of a transmission system. Petry-Johnson et al. [5]

have shown the influence of surface roughness and a formed thin lubricant film in gear teeth pair conjunctions upon generated friction and eventually the efficiency of a gear box operating at speeds up to 10,000 rpm. Li and Kahraman [6] developed a tribodynamic model to predict friction throughout a meshing cycle of a spur gear pair. Using theoretical tooth profiles, the authors showed the essential coupling between gear dynamics and tribology of contact throughout the meshing cycle. There have been other contributions with a focus on spur gear pairs [7–10].

Two key factors influence the structural integrity of teeth–pair contacts. These are the induced root stresses and contact surface defects caused by the generated sub-surface stresses. The latter form part of the current investigation, as they are more of concern for high-performance transmissions based upon spur gears. It has been shown that the onset of fatigue spalling is a crucial problem in spur gears and is generally induced by generated high sub-surface shear stresses [11–14]. However, an important issue is the proper consideration for the determination of real contact surface geometry and kinematics, as well as an accurate lubrication model, which are the main contributions of the current paper.

Traditionally, the contact parameters used for the tribological studies are obtained using Tooth Contact Analysis (TCA) [1,15–18]. However, the traditional TCA approach assumes perfect geometry of the contacting teeth under dry contact conditions. Consequently, surface defects from manufacturing processes or those caused during operation are not taken into account. Surface defects result in some changes in surface geometry and thus the contact conditions. Furthermore, gear teeth contacts are lubricated. These issues were recently taken into account by Oglieve et al. [19] in the reported Lubricated Loaded Tooth Contact Analysis (LLTCA) approach, which is adopted here. Details and procedures in this regard are highlighted in Section 2.1.

In order to evaluate the effect of LLTCA alone, the current study uses a standard one-dimensional non-Newtonian thermoelastohydrodynamic lubrication (TEHL) model of spur gear teeth pair with the instantaneous contact geometry and kinematics determined using the LLTCA, which is compared with the traditional TCA method. In this manner, the effect of LLTCA in a more accurate prediction of contact conditions becomes clear. Such an approach has not hitherto been reported in the literature.

2. Methodology

2.1. Tooth Contact Analysis (TCA) and Lubricated Loaded Tooth Contact Analysis (LLTCA)

There is a significant volume of work reported on gear design, research, and development, including in [20–22]. They show that the kinematics of gears, particularly for racing transmissions, require inclusion in the analysis [15,23]. Contact kinematics and geometry influence the contact loading of engaged teeth and consequently affect lubricant film formation, viscous shear, and friction. Therefore, there is a need for a TCA tool at the outset of any tribological study to provide the geometry and contact kinematics. The traditional TCA method was developed by Litvin and Fuentes [15] and Vijayakar [16], which are currently well-established and widely used. For this paper, the results from CALYX [16] are used to represent the TCA approach. As Oglieve et al. [19] showed, most FEA models solving complex contact problems such as the meshing gear teeth fail to consider lubricated surfaces, coupled with realistic surface geometry, which is measured directly using a coordinate measuring machine (CMM). The LLTCA approach aims to overcome this problem by introducing real geometry, coupled with realistic friction derived from a lubrication model. The key differences between TCA and LLTCA are summarized in Figure 1.

Figure 1 shows the main differences between LLTCA and TCA as the introduction of real surface geometry and lubricated contact by the former approach, as opposed to the ideally perfect and dry contact geometry by the latter. An overview on the process involved with LLTCA is shown in Figure 2. A comprehensive explanation of the process shown in Figure 2 has already been given in [19]. However, briefly, it can be noted that the process involves acquiring kinematic and kinetic data from the finite element analysis for each meshing point, and subsequently, friction in the contact is updated

based on Equation (1). The results are entered into the software, and the process is repeated until the generated friction converges within an acceptable error tolerance.

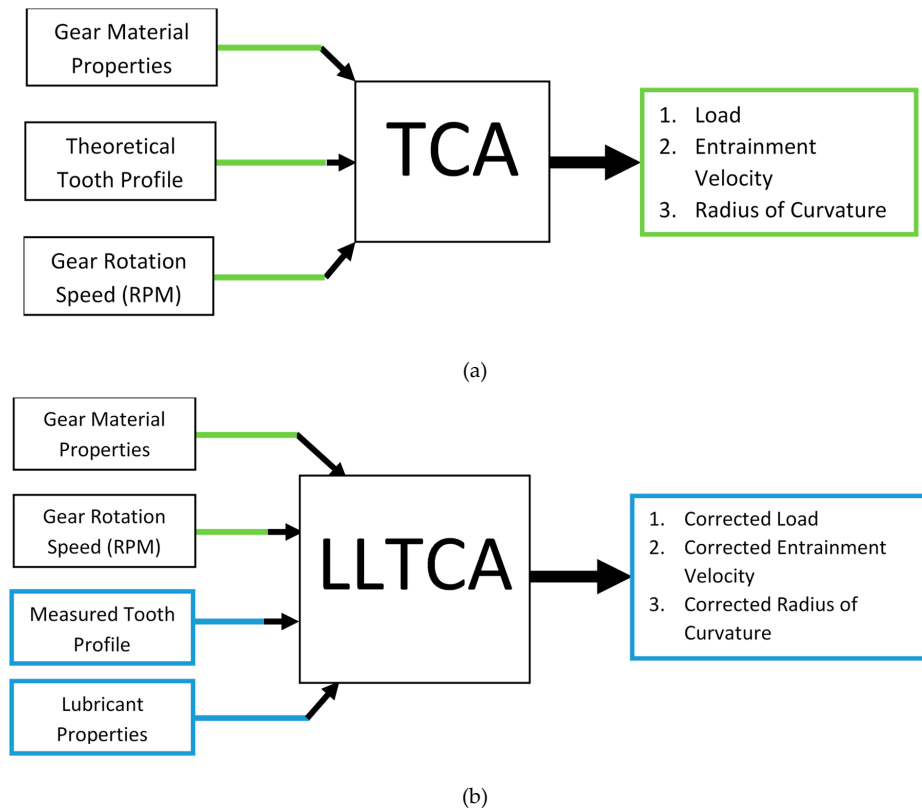


Figure 1. Overview of (a) Tooth Contact Analysis (TCA) and (b) Lubricated Loaded Tooth Contact Analysis (LLTCA).

Surface geometry used for the analysis is measured using a coordinate measuring machine (CMM) with a measurement sensitivity of $\pm 1.5 \mu\text{m}$. This allows for the inclusion of realistic surface defects/anomalies in the analysis. The coefficient of friction, fed back into the LLTCA's FEA solver, is determined using a relationship provided by Evans and Johnson [24] as:

$$\mu = 0.87\bar{\alpha}\tau_0 + 1.74\frac{\tau_0}{\bar{p}} \ln \left[\frac{1.2}{\tau_0 h_c} \left(\frac{2k_l \eta_0}{1 + 9.6\zeta} \right)^{1/2} \right] \quad (1)$$

where:

$$\zeta = \frac{4k_l}{\pi h_c / R'} \left(\frac{2\bar{p}}{E' k_s R' \rho' c' \bar{U}} \right)^{1/2} \quad (2)$$

p_{avg} and τ_0 are the average contact pressure and characteristic (Eyring) shear stress of the lubricant, respectively. The density and specific heat of the gear material are denoted by ρ_g and c_g .

The lubricant film thickness at the center of the contact is predicted using the extrapolated oil film thickness formula of Chittenden et al. [25]:

$$h_c = H_c R \quad (3)$$

where;

$$H_c = 4.31U^{*0.68}G^{*0.49}W^{*-0.073} \left[1 - \exp \left(-1.23 \left(\frac{r_y}{r_x} \right)^{2/3} \right) \right] \quad (4)$$

in which the non-dimensional parameters are $G^* = \alpha_0 E'$, $U^* = \eta_0 U / 2E'R$, and $W^* = W / E'R'^2$.

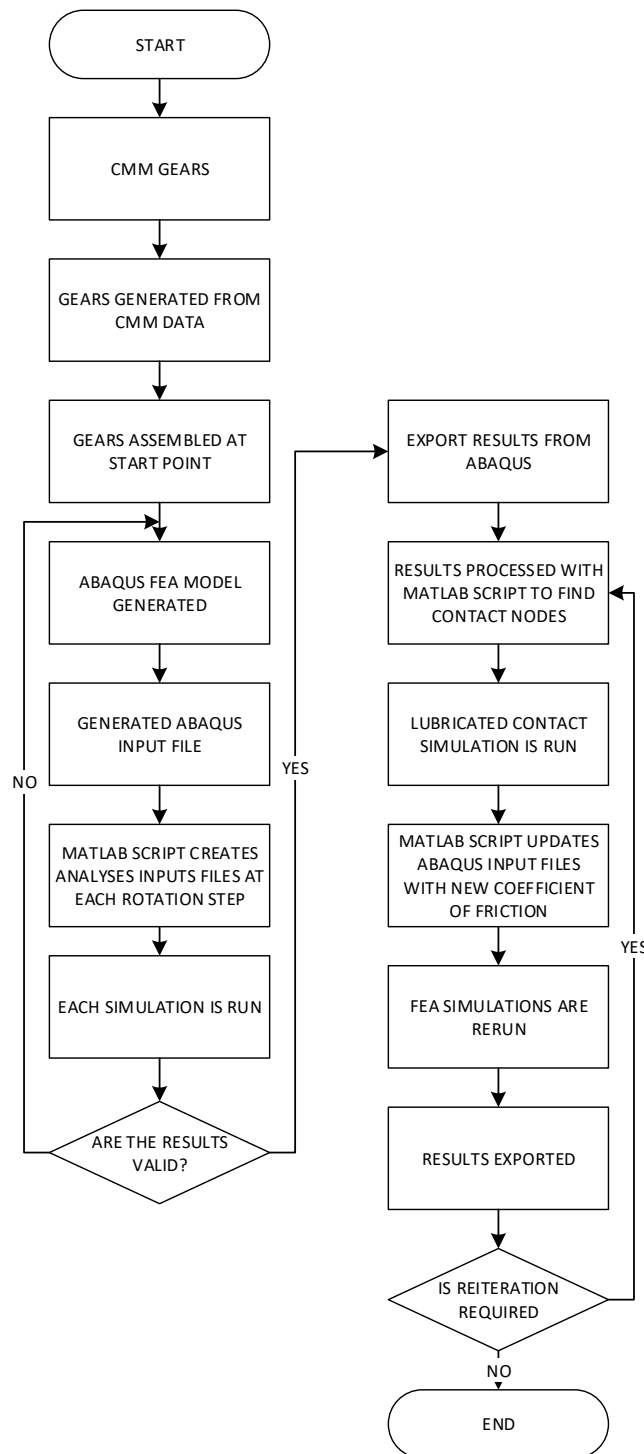
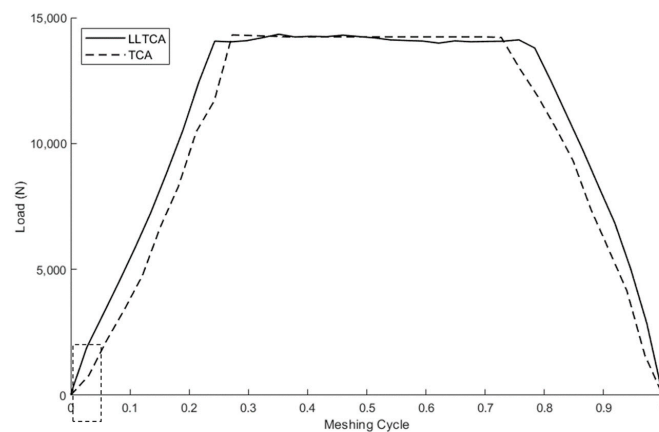


Figure 2. LLTCA procedure flow chart [19].

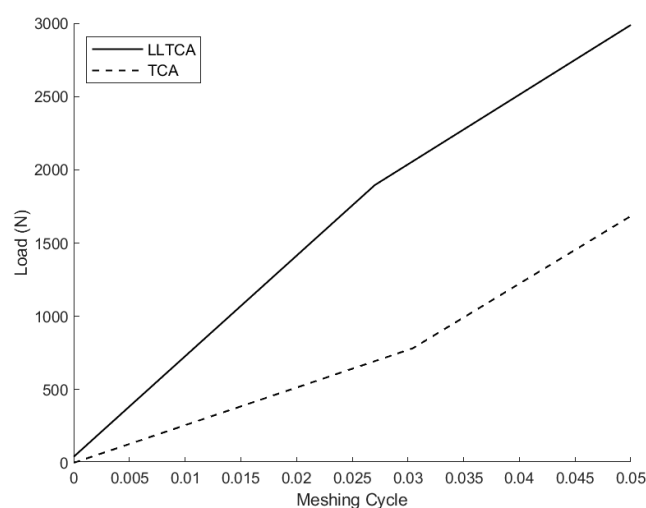
It is assumed that all gear teeth would undergo the same loading history during a typical meshing cycle. Thus, to reduce the burden of computation, only three consecutive teeth pair meshing cycles are modeled. This enables the development of a detailed model by setting the computational domain according to the trailing, current, and leading meshing teeth pairs only. Moreover, this investigation looks at a single meshing cycle. Ideally, to fully incorporate thermal effects, more than one cycle would need to be considered. In addition, a thermal network model coupled

with the elastohydrodynamic lubrication (EHL) solver, which is presented later, can be embedded into the LLTCA method explained above in order to provide a more precise LLTCA analysis. However, this would be highly computationally resource-intensive and goes beyond the scope of the current investigation. Thus, the presented methodology is deemed as satisfactory.

The gear pair and operating conditions investigated by Oglieve et al. [19] are used in the current paper. The applied torque and rotational speed applied to the pinion was 312 Nm and 11,758 rpm, respectively [19]. Further details are outlined in Appendix A. It is noteworthy that a typical simulation based on the use of traditional TCA would take considerably less time than one adopting the new LLTCA approach. However, the results of LLTCA are much more representative of realistic conditions encountered in practice. Furthermore, refined and improved methods of computation can be developed to improve upon the computation times for the LLTCA. The most important results for the entire meshing cycle are the generated contact loads, as well as the speed of the entraining motion of the lubricant into the conjunction of a meshing teeth pair (i.e., the average speed of moving mating surfaces), as illustrated in Figures 3 and 4, respectively. Figure 3b shows that LLTCA predicts an earlier engagement at the onset of meshing. Thus, the start and the end of a meshing cycle differs for the LLTCA and TCA methods.



(a)



(b)

Figure 3. (a) Contact force through the meshing cycle, (b) Detailed view [19].

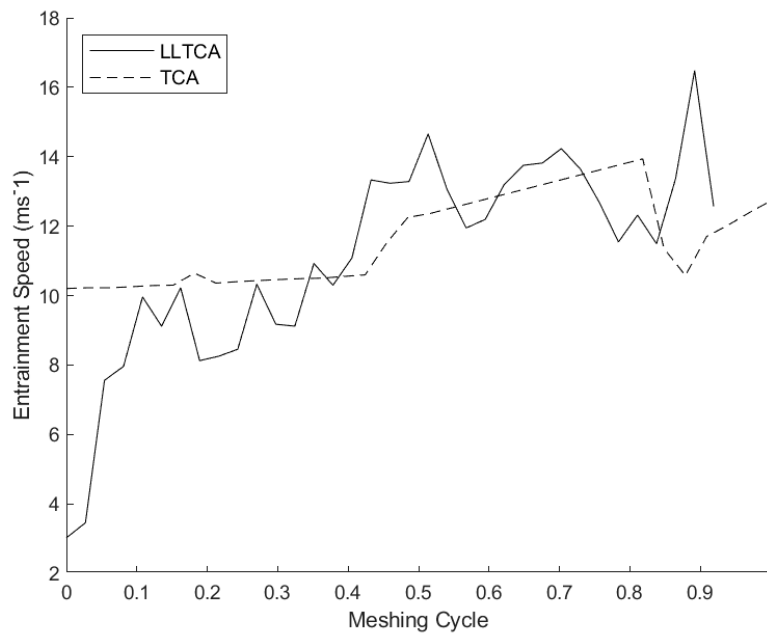


Figure 4. Entrainment speed through the meshing cycle [19].

2.2. Elastohydrodynamic Lubrication (EHL)

High-performance spur gears exhibit contact pressures in excess of 1.2 GPa [18,22]. Therefore, the contact conditions pertain to a viscous–elastic (i.e., elastohydrodynamic) regime of lubrication. To obtain the pressure distribution and the corresponding film thickness, a simultaneous solution of Reynolds equation, elastic film shape, and lubricant rheological state equations is required.

In order to evaluate the effect of LLTCA alone, when compared with TCA, a well-established EHL analysis approach is followed.

The general form of Reynolds equation is:

$$\frac{\partial}{\partial x} \left[\frac{\rho h^3}{6\eta} \left(\frac{\partial p}{\partial x} \right) \right] + \frac{\partial}{\partial y} \left[\frac{\rho h^3}{6\eta} \left(\frac{\partial p}{\partial y} \right) \right] = \frac{\partial(\rho h U)}{\partial x} + \frac{\partial(\rho h V)}{\partial y} + \frac{\partial(2\rho h)}{\partial t} \quad (5)$$

where p , h , η , and ρ are the pressure, film thickness, lubricant dynamic viscosity, and density, respectively. U and V are surface velocities along the direction of entraining motion, x , and in the side-leakage direction, y , respectively. Olver [26] showed that spur gears generally run starved. Therefore, it can be assumed that the effect of lubricant side leakage would be negligible (i.e., $V = 0$). Therefore, a one-dimensional (1D) EHL solution would suffice. Furthermore, a quasi-static analysis of a meshing cycle is carried out. Therefore, the effect of squeeze film motion $\partial(2\rho h)/\partial t$ is neglected. A more comprehensive approach would require the effect of transience through the inclusion of squeeze film terms as an extension of the current analysis. This simplifies the Reynolds equation to:

$$\frac{\partial}{\partial x} \left[\frac{\rho h^3}{6\eta} \left(\frac{\partial p}{\partial x} \right) \right] = \frac{\partial(\rho h U)}{\partial x}. \quad (6)$$

The elastic film shape is given as:

$$h = h_0 + s(x) + \delta(x) \quad (7)$$

where h_0 is the minimum film thickness (rigid clearance), s is the geometric profile of the teeth pair conjunction, and δ is the localized elastic deflection. It is apparent that the aspect ratio of the contact

footprint would be high for spur gear teeth pair conjunctions. Therefore, for the case of an undeformed line contact, the profile of an equivalent solid near a semi-infinite elastic half-space becomes [27]:

$$s(x) = \frac{x^2}{R'} \quad (8)$$

The equivalent radius of curvature R' of the equivalent solid is taken from LLTCA. The general form of the localized elastic deflection is given by the elasticity potential equation as [28]:

$$\delta(x, y) = \frac{4}{\pi E'} \int p(x') \ln(x - x') dx' \quad (9)$$

Due to the high entrainment speed in very narrow conjunctions of gear contacts, it is necessary to consider a non-Newtonian viscosity model. To incorporate the effect of shear thinning, a similar approach to that of Paouris et al. [29] is undertaken, using the Havriliak and Negami [30] rheological model:

$$\eta = \frac{\eta_0}{F(\lambda)} \quad (10)$$

where the rest viscosity, η_0 , is taken at ambient pressure. The non-Newtonian function, $F(\lambda)$, and shear rate, $\dot{\gamma}$, are given as:

$$F(\lambda) = \left[1 + (\lambda \dot{\gamma})^{\alpha_{HN}} \right]^{\beta_{HN}} \quad (11)$$

$$\dot{\gamma} = \frac{\Delta U}{h_c} \quad (12)$$

where λ , α_{HN} , and β_{HN} are the lubricant's specific parameters found experimentally [30]. The shear rate is calculated using the lubricant film thickness at the center of the meshing teeth pair contact domain, h_c .

For the majority of the meshing cycle (as shown later in the results), the contact undergoes a viscoelastic regime of traction [24], with lubricant viscosity being highly dependent on the generated contact pressures. Therefore, the Havriliak and Negami model [30] needs to be adjusted accordingly as:

$$\eta = \frac{\eta_p}{F(\lambda)} \quad (13)$$

where η_p can be found using the following expression [31]:

$$\eta = \eta_0 \exp \left\{ \ln \left(\frac{\eta_0}{\eta_r} \right) \left[\left(1 + \frac{p}{p_r} \right)^Z - 1 \right] \right\} \quad (14)$$

Constants η_r and p_r are 6.31×10^{-5} and 1.9609×10^8 , respectively and the piezoviscosity index, Z , can be found from:

$$Z = \frac{\alpha_0 p_r}{\ln \left(\frac{\eta_0}{\eta_r} \right)} \quad (15)$$

where the pressure–viscosity coefficient, α_0 , is usually obtained through experimental measurements.

As it will be shown later, some regions of the meshing cycle can be shear-independent. In these regions $F(\lambda) = 1$, resulting in lubricant viscosity being solely dependent on generated pressure (i.e., only Equation (14) is used).

The rest viscosity of the lubricant, η_0 , is temperature-dependent and is found using the Vogel's equation [32]:

$$\eta_0 = a_v \exp \left(\frac{b_v}{T - c_v} \right) \quad (16)$$

where, a_v , b_v , and c_v are lubricant-specific constants found through measurements of viscosity at three different temperatures and through subsequent curve-fitting [33,34].

The effect of pressure and temperature on lubricant density is also taken into account as [35]:

$$\rho = \rho_0 \left(1 + \frac{0.6 \times 10^{-9} p}{1 + 1.7 \times 10^{-9} p} \right) \left[1 - 0.65 \times 10^{-3} (T - T_0) \right] \quad (17)$$

where the density at ambient temperature and pressure is denoted by ρ_0 . Reference and bulk temperatures are denoted as T_0 and T , respectively.

2.3. Tractive Analysis

To undertake analysis which is representative of in situ gear meshing conditions, it is essential to determine the prevailing regime of lubrication as well as the tractive conditions. To determine the regime of lubrication, the Greenwood chart is used [36]. Figure 5 shows the Greenwood chart, where the non-dimensional parameters are:

$$G_e = \frac{W^* \frac{8}{3}}{U^{*2}} \quad (18)$$

$$G_v = \frac{G^* W^{*3}}{U^{*2}} \quad (19)$$

where $G^* = \alpha_0 E'$, $U^* = \eta_0 U / 2E'R$, and $W^* = W / E'R'l$.

Figure 5 shows the meshing cycle conditions according to the results of the current LLTCA and TCA analyses. It is clear that in both cases, piezoviscous-elastic (i.e., EHL) is the prevailing regime of lubrication. The meshing cycle commences with a tip-to-root teeth-pair interactions at low load with LLTCA, resulting in isoviscous rigid (i.e., hydrodynamics). It is often the case that the gear relief profile inhibits interactions in this region. Therefore, the current analysis ignores interactions in this region of the meshing cycle.

Often, the thin elastohydrodynamic films formed in the gear teeth meshing at high loads and/or shear cause viscoelastic traction with shear stress exceeding the limiting Eyring shear of the lubricant, which can subsequently reduce due to increased contact temperature [34]. One way of ascertaining any non-Newtonian viscous shear of the lubricant is to use the Deborah number, D [37] as:

$$D = \frac{\eta(p, T) U}{2bG} \quad (20)$$

where G is the lubricant shear modulus and is obtained as [38]:

$$G = (G_0 + \alpha_0 p) e^{\beta_0 \left(\frac{1}{T} - \frac{1}{T_0} \right)} \quad (21)$$

where G_0 is the atmospheric shear modulus of the lubricant and β_0 is the thermoviscosity index. Non-Newtonian viscoelastic traction is expected when $D > 1$.

Figure 6 shows the variation of Deborah number in the contact of a pair of spur gear teeth during a meshing cycle with contact geometry and kinematics determined through LLTCA and TCA methods. A bulk lubricant temperature of 40 °C is chosen to simulate cold start-up conditions where shear thinning behavior is dominant.

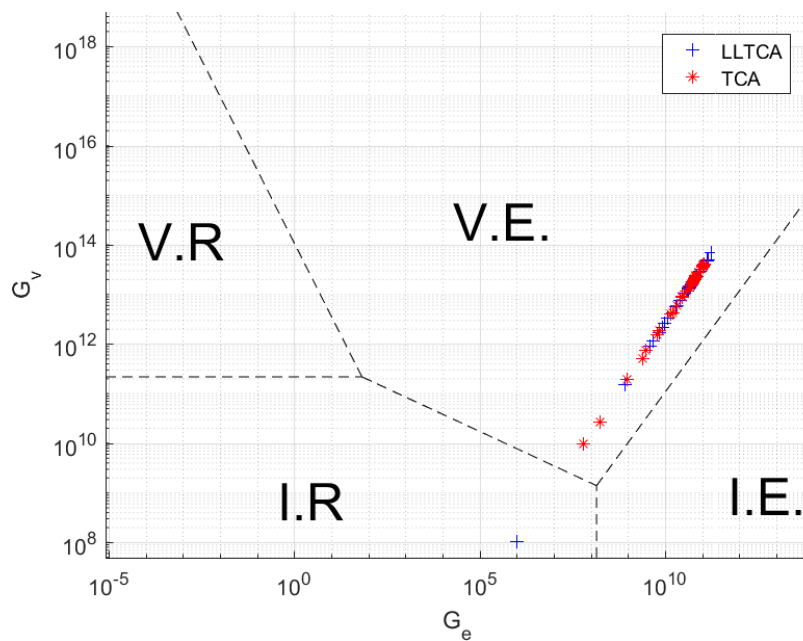


Figure 5. Meshing cycle on the Greenwood Chart: I.R.—Isoviscous Rigid, V.R—Piezoviscous Rigid, I.E.—Isoviscous Elastic, V.E.—Piezoviscous Elastic [38].

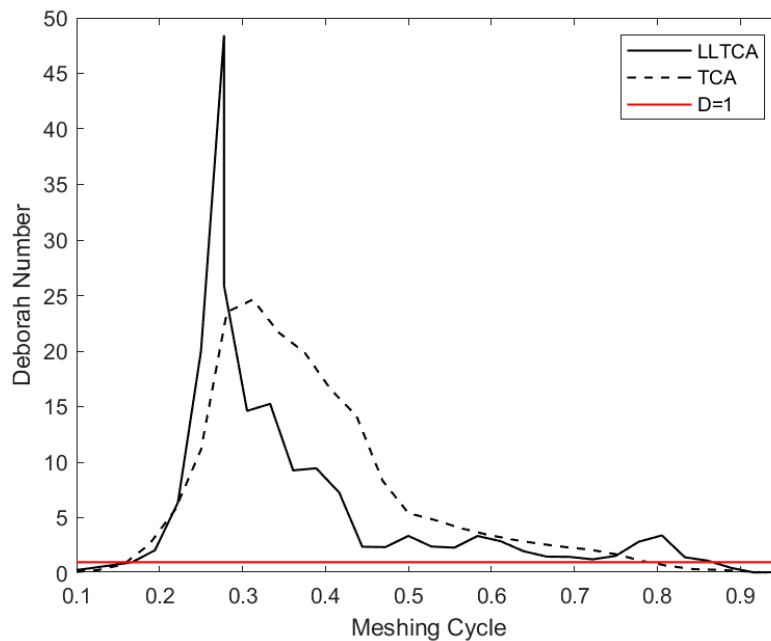


Figure 6. Variation of Deborah number during a meshing cycle with input data predicted through LLTCA and TCA.

The results show that the Deborah number exceeds the value of unity for most of the meshing cycle, with parts of the meshing cycle being $D > 20$ for the case of LLTCA. This strongly suggests that the lubricant film is subject to non-Newtonian shear throughout the meshing cycle [34,37]. Additionally, it is shown later that the film thickness values under the specified operating conditions yield Stribeck’s lubricant film ratios exceeding the limit for the onset of mixed regime of lubrication. Therefore, the effect of surface roughness is not considered in the current analysis.

2.4. Thermal Network Model

Aside from shear thinning due to non-Newtonian lubricant behavior, another salient feature of the high-performance spur gear transmission system is thermal shear heating and the conduction of heat through the solid boundaries. Therefore, it is essential to carry out a thermo-elastohydrodynamic analysis, which can be carried out analytically through the development of a thermal network model. The thermal network model is used to calculate the average temperature of the contact and the rise in surface temperature of the contacting solids (i.e., meshing teeth) from a cold start-up condition. The methodology is adopted from the original work of Morris et al. [39].

Rate of friction-induced heat generation, \dot{Q} , is obtained as:

$$\dot{Q} = f_r \Delta U. \quad (22)$$

This heat is conducted away through the contacting surfaces of the meshing teeth pair with the rate of \dot{Q}_1 and \dot{Q}_2 , respectively. The remainder of the heat is carried away by the lubricant through convection, \dot{Q}_{cv} . However, it is shown that the convective heat removal rate, \dot{Q}_{cv} is almost negligible in EHL contacts due to the thinness of the lubricant film and its low flow rate [34,40,41]. However, convective heat transfer by the lubricant flow is retained here for the sake of completeness of the analysis. Thus, the thermal energy equilibrium dictates that:

$$\dot{Q} = \dot{Q}_1 + \dot{Q}_2 + \dot{Q}_{cv}. \quad (23)$$

Considering the inlet heating effect, the lubricant bulk flow temperature, θ_0 , is calculated considering an initial solid body temperature of 40 °C, thus:

$$\theta_0 = \frac{\theta_{s1}U_1 + \theta_{s2}U_2}{U_1 + U_2}. \quad (24)$$

\dot{Q}_{cv} is obtained as:

$$\dot{Q}_{cv} = \dot{m}c_p(\theta_e - \theta_0). \quad (25)$$

where θ_e is the effective contact temperature and c_p is the specific heat capacity of the lubricant, and its mass flow rate is found as [42]:

$$\dot{m} = -\frac{\rho_c h_c^3}{12\eta_c} \left(\frac{\partial p}{\partial x} \right) + U \left(\frac{\rho_c h_c}{2} \right) \quad (26)$$

where h_c , η_c , and ρ_c are the lubricant film thickness, viscosity, and density at the center of the contact, respectively.

A more accurate thermal EHL analysis would require consideration of two-phase flow, taking into account the effect of cavitation. However, this is beyond the scope of the current analysis. As Morris et al. [39] and Paouris et al. [40] have noted, the heat flowing to the bounding contacting surfaces would need to overcome several thermal resistive barriers, as illustrated in Figure 7. Therefore, an analytical approach based on a thermal network model is deemed to be suitable for the purpose of the current study.

From Figure 7, it can be deduced that

$$R_i = R_{l_i} + R_{f_i}, \quad i = 1, 2 \quad (27)$$

where R_{l_i} and R_{f_i} are the thermal resistances due to the lubricant film and the flash temperature rise of the solid surfaces. Resistances R_{l_i} , R_{f_i} , and R_e can be obtained as follows:

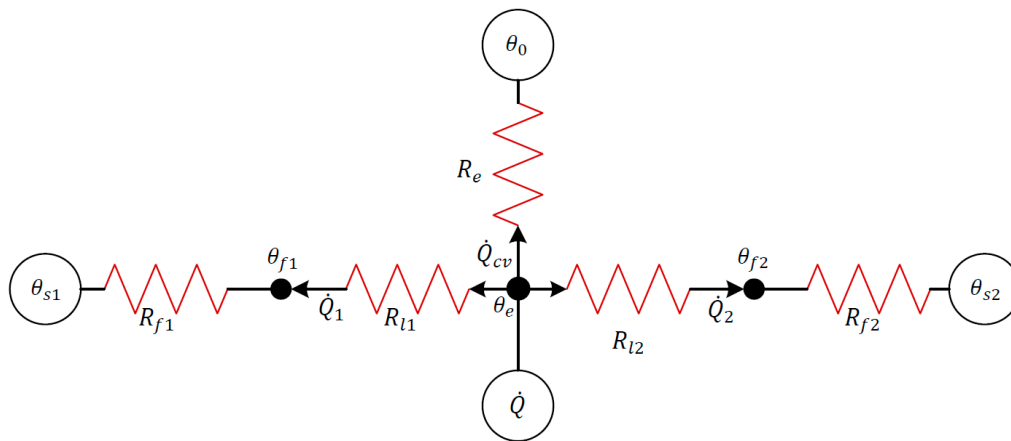


Figure 7. The thermal network model [39].

In the current analysis, it is assumed that the generated heat takes place at the center of the contact. Therefore, the generated heat is conducted away through the lubricant layer adjacent to the contacting surfaces. The lubricant film thickness would be half that of the central film; thus, the corresponding thermal resistance becomes [40]:

$$R_{l_i} = \frac{h_c}{2k_l A_{EHL}}. \quad (28)$$

The thermal resistance considering the flash temperature of solid surfaces is obtained as [41]:

$$R_{f_i} = \frac{1.06 S_{f_i}}{k_s A_{EHL}}. \quad (29)$$

As noted earlier, the effect of heat convected away from the contact due to the mass flow rate of the lubricant through the contact is usually neglected due to the thinness of an EHL film. Nevertheless, for the sake of completeness, the equivalent thermal resistance due to mass flow rate of lubricant is given as [39]:

$$R_e = \frac{1}{\dot{m} c_p}. \quad (30)$$

The contact area A_{EHL} is simply $2bl$, where b and l are the Hertzian contact width and length, respectively. Moreover, S_{f_i} is found as [42]:

$$S_{f_i} = \sqrt{\frac{2k_s b}{\rho_s c_s \Delta U}}, \quad i = 1, 2. \quad (31)$$

Therefore, the heat conducted away through the gear blanks can be stated as

$$\dot{Q}_i = \frac{\theta_e - \theta_i}{R_i}, \quad i = 1, 2. \quad (32)$$

Thus, the heat balance Equation (23) takes the form:

$$\dot{Q} = \frac{\theta_e - \theta_1}{R_1} + \frac{\theta_e - \theta_2}{R_2} + \frac{\theta_e - \theta_0}{R_e}. \quad (33)$$

The average (effective) contact temperature can now be determined as:

$$\theta_e = \left[\dot{Q} + \left(\frac{\theta_1}{R_1} + \frac{\theta_2}{R_2} + \frac{\theta_0}{R_e} \right) \right] \left(\frac{1}{R_1} + \frac{1}{R_2} + \frac{1}{R_e} \right)^{-1}. \quad (34)$$

Once the effective temperature in the contact is determined, the temperature rise in the contacting solid surfaces and the lubricant exiting the contact can be determined using the heat partitioning method [39] illustrated in Figure 7. The thermal partition coefficient, χ_i for the bodies and lubricant can be found as:

$$\frac{\dot{Q}_i}{\dot{Q}} = \chi_i = \frac{\theta_e - \theta_i}{\dot{Q}R_i}, i = 1, 2 \quad (35)$$

and

$$\chi_3 = 1 - (\chi_1 + \chi_2) = \frac{\theta_e - \theta_0}{\dot{Q}R_e}. \quad (36)$$

Using Equations (35) and (36), surface temperature rise can be obtained as:

$$\Delta\theta_i = \frac{S_{f_i}}{k_s A_{EHL}} \chi_i \dot{Q}. \quad (37)$$

Note that it is assumed that the temperature calculated at each preceding meshing point neither influences the temperature of any subsequent meshing point nor the bulk gear temperature, as it is expected that a meshing cycle is completed prior to any rise in the bulk gear body being noted. This assumption is considered reasonable, since the Peclet number (the ratio of convective to conductive heat transfer) throughout the meshing cycle remains quite small (between 0.056 and 0.14). Furthermore, the study is concerned with the contact between a single gear teeth pair, taking place in a very short interval of time (a single engagement instant merely lasts 2.26×10^{-6} s).

3. Method of Solution

The unknowns in the analysis are pressure, viscosity, density, localized contact deflection, lubricant film thickness, and temperature. The number of unknowns is equal to the number of equations at each instant of meshing. However, due to the non-linear nature of the relationships, it is necessary to use an iterative numerical technique to solve the thermo-EHL problem. The Effective Influence Newton–Raphson (EIN) method is used for discretization of Reynolds equation through a distributed line relaxation algorithm [43]. This technique is well-established for solving EHL contact problems, especially those subjected to high loads.

The following procedure is used:

1. Inputs from LLTCA at the start of the meshing cycle are used.
2. An initial guess is made for the film thickness at the center of the contact.
3. The computational domain is set with an inlet length of $12.42b$ and contact exit position of $4.42b$. The number of elements used in the direction of lubricant entrainment is 2051.
4. Iterative pressure residuals are found using the under-relaxed Effective Influence Newton (EIN) method, including local surface deflection calculated through the use of Equation (9), which is based on Equation (38), where n denotes the iteration step and Ω is the under-relaxation factor, typically 10^{-2} – 10^{-1} :

$$p^n = p^{n-1} + \Omega \Delta p^n. \quad (38)$$

5. The iterative procedure evaluates the contact pressure and continues until the pressure convergence criterion is satisfied:

$$\sum_i \sum_j \left| \frac{p_{i,j}^n - p_{i,j}^{n-1}}{p_{i,j}^n} \right| \leq 10^{-3}. \quad (39)$$

6. When pressure convergence is satisfied, the contact load-carrying capacity is calculated through the integration of pressure distribution over the computational domain as:

$$W_p = \int p dx. \quad (40)$$

7. The following equilibrium condition should be satisfied in order to achieve a load balance condition where W is the applied load:

$$\left| \frac{W - W_p}{W} \right| \leq 10^{-3}. \quad (41)$$

8. If Equation (41) is not satisfied, the film thickness is updated through modification of the undeformed gap, using Equation (42):

$$h_0 = h_0 \left(\frac{W_f}{W} \right)^\zeta. \quad (42)$$

where ζ is termed the damping (load relaxation) factor, and for the current analysis, the value of 10^{-3} is used. Subsequently, the density and viscosity are updated using the newly found pressure. Then, Steps 4 to 8 are repeated until Step 7 is satisfied.

9. Once the film thickness is determined, the thermal network model (highlighted in Section 2.4) is used to find the temperature of the lubricant as well as those of the adjacent meshing surfaces.
10. Steps 2 to 9 are repeated for each point on the meshing cycle until the entire meshing cycle is completed.

4. Shear Stress and Friction

Friction is determined as:

$$f_r = \tau A_{EHL} \quad (43)$$

where the shear stress, τ , for conventional Newtonian shear is given as:

$$\tau = \pm \frac{h}{2} \frac{\partial p}{\partial x} + \frac{\eta \Delta U}{h}. \quad (44)$$

However, as Paouris [29] noted, when the lubricant behaves in a non-Newtonian manner, then shear stress is given as:

$$\tau = \frac{\eta}{F(\lambda)} \dot{\gamma}. \quad (45)$$

Equation (45) is used when the Deborah number exceeds unity. Otherwise, shear stress is defined by Equation (44). This condition is deemed to occur as the calculated shear exceeds the Eyring shear stress of the lubricant, τ_0 (i.e., $\tau > \tau_0$) [24,34,44,45]. Then, the shear stress becomes dependent on pressure and is found as:

$$\tau_l = \tau_0 + \gamma \bar{p} \quad (46)$$

where \bar{p} is the average contact pressure and γ is the limiting shear strength proportionality constant. The constant γ is found experimentally [45] and is usually in the range of 0.026–0.14, depending on the lubricant. In this investigation, $\gamma = 0.029$.

5. Sub-Surface Stress Field

Fatigue spalling is a determining factor for the structural integrity of gearing systems. In a mixed regime of lubrication, the asperities on the opposing contacting surfaces can interact and cause surface wear and/or fatigue. However, in a pure EHL contact, which is the case assumed here, the root cause of fatigue emanates through sub-surface stresses reaching certain limits in the presence of sub-surface flaws. Therefore, it is important to predict the likelihood of onset of fatigue spalling in such cases. This is usually caused by the coupling of high generated contact pressures and shear [11,34,46]. In the

absence of any surface coating, the approach adopted by Johnson [47] is commonly used to calculate the sub-surface stresses induced by pressure and shear under EHL conditions:

$$\sigma_x = -\frac{2z}{\pi} \int_{-fi}^{fo} \frac{p(s')(x-s')^2 ds'}{[(x-s')^2 + z^2]^2} - \frac{2}{\pi} \int_{-fi}^{fo} \frac{q(s')(x-s')^3 ds'}{[(x-s')^2 + z^2]^2} \quad (47)$$

$$\sigma_z = -\frac{2z^3}{\pi} \int_{-fi}^{fo} \frac{p(s') ds'}{[(x-s')^2 + z^2]^2} - \frac{2z^2}{\pi} \int_{-fi}^{fo} \frac{q(s')(x-s') ds'}{[(x-s')^2 + z^2]^2} \quad (48)$$

$$\tau_{xz} = -\frac{2z^2}{\pi} \int_{-fi}^{fo} \frac{p(s')(x-s') ds'}{[(x-s')^2 + z^2]^2} - \frac{2z}{\pi} \int_{-fi}^{fo} \frac{q(s')(x-s')^2 ds'}{[(x-s')^2 + z^2]^2} \quad (49)$$

where s' is the intermediate parameter along the x -coordinate on the computational domain and z is the Cartesian coordinate into the depth of the contacting solids. Viscous shear stress in the x -direction, $q(s')$, on the lower surface is obtained as:

$$q(s') = \tau. \quad (50)$$

It must be noted that a 2D sub-surface analysis approach should consider both shear stress in the direction of entrainment and pressure orthogonal to the surface; thus, the approach expounded here is quite suitable for the idealized 1D infinite line contact EHL. However, a more comprehensive approach would require a full 3D analysis, particularly for the case of finite line contacts. The computational domain for the sub-surface stress field is the same as that used for the evaluation of the generated pressures. The dimension into the depth of contacting solids uses a length of $10b$ and 1000 elements are used along the z -axis. The sub-surface stress solver utilizes a trapezoidal numerical integrator.

For gears and bearings made of ductile material, failure is usually governed by cyclic reversing orthogonal shear stresses, τ_{xz} , as shown by various authors [34,48–50].

6. Results and Discussion

The current investigation focuses on the high-performance transmissions of race vehicles. Therefore, the material and lubricant properties are chosen accordingly. An important point to note is that the surface topography is very smooth (of the order of 0.05–0.1 μm). Therefore, there is no need to consider boundary friction as well as surface fatigue, which would otherwise be required for the direct contact of rough surfaces in more conventional gearing systems. Table 1 lists the surface material and lubricant rheological data. The lubricant is considered to have similar shear thinning characteristics as those described by Paouris et al. [50]; thus, λ , α_{HN} and β_{HN} have been chosen accordingly and are included in Table 2.

Table 1. Lubricant base properties [22].

Parameter	Symbol	Value	Units
Young's modulus (both pinion and wheel)	E_1, E_2	206	GPa
Poisson ratio (both pinion and wheel)	ν_1, ν_2	0.3	-
Dynamic viscosity (at 40 °C)	η_0	0.0304	Pa·s
Lubricant density (at 40 °C)	ρ_0	851	kg/m ³
Pressure coefficient of viscosity (at 40 °C)	α_0	1.69×10^{-8}	1/Pa
Density of the solid	ρ'	7800	kg/m ³
Limiting shear stress	τ_L	2	MPa
Specific heat capacity of lubricant	c_p	1670	J/kg·K
Specific heat capacity of solid	c_s	470	J/kg·K
Thermal conductivity of lubricant	k_l	0.137	W/m·K
Thermal conductivity of the solid	k_s	46.7	W/m·K

Table 2. Non-Newtonian lubricant properties [50].

Parameter	Value	Units
λ_f	7.9×10^{-8}	S
α_{HN}	0.7	-
β_{HN}	1	-

Figure 8 shows a comparison of the predicted minimum film thickness during a meshing cycle, using the geometrical and kinematic data obtained through use of LLTCA and the conventional TCA. Despite the difference in the speed of lubricant entrainment and the contact radii of curvature, the lubricant film thickness remains almost unaltered between the two cases. However, at the start and the end of a meshing cycle, use of the TCA data appears to show a thicker film thickness value compared with that using the LLTCA data. The thinner film thickness predicted by the LLTCA case suggests that the inlet would move closer to the contact center, resulting in starvation during the early and later stages of the meshing cycle, which explains the reason for the insensitivity to lubricant entraining speed.

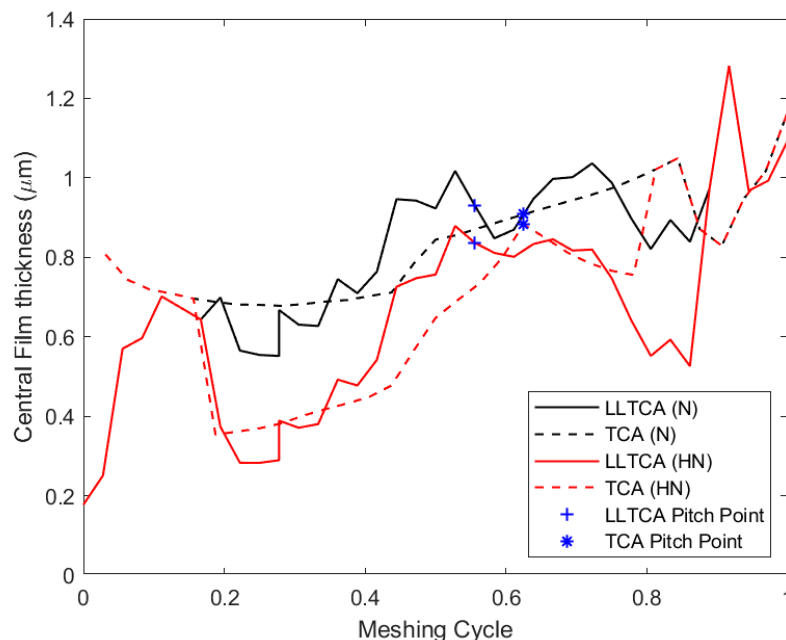


Figure 8. Central contact thickness across the meshing cycle: N—Newtonian, HN—Havriliak, and Negami shear thinning.

The introduction of shear thinning originated from the non-Newtonian behavior of the lubricant has a significant effect on the lubricant film thickness. Figure 8 clearly illustrates the transition between Newtonian and non-Newtonian lubricant shear behavior with a sudden reduction in lubricant film thickness. Up to a 50% difference between Newtonian and non-Newtonian behavior for LLTCA and 48% for the case of TCA are noted. At the pitch point, there is no relative velocity between the contacting surfaces (i.e., pure rolling). With no sliding speed, the shear thinning effect is reduced, thus resulting in an increase in the thickness. However, even at low sliding speeds, the shear thinning effect has a significant influence on film thickness. With the LLTCA input conditions, at the pitch point, there is a reduction of 13%.

Figure 9 shows the change in pressure and film thickness between Newtonian and non-Newtonian behavior, including the effect of shear thinning. These results correspond to isothermal conditions at 40 °C. Clearly, the change in film thickness is the result of non-Newtonian shear thinning, reducing the

lubricant film availability for entrainment into the contact. The pressure distribution remains unaltered as EHL films are insensitive to load, which primarily determines the generated pressures.

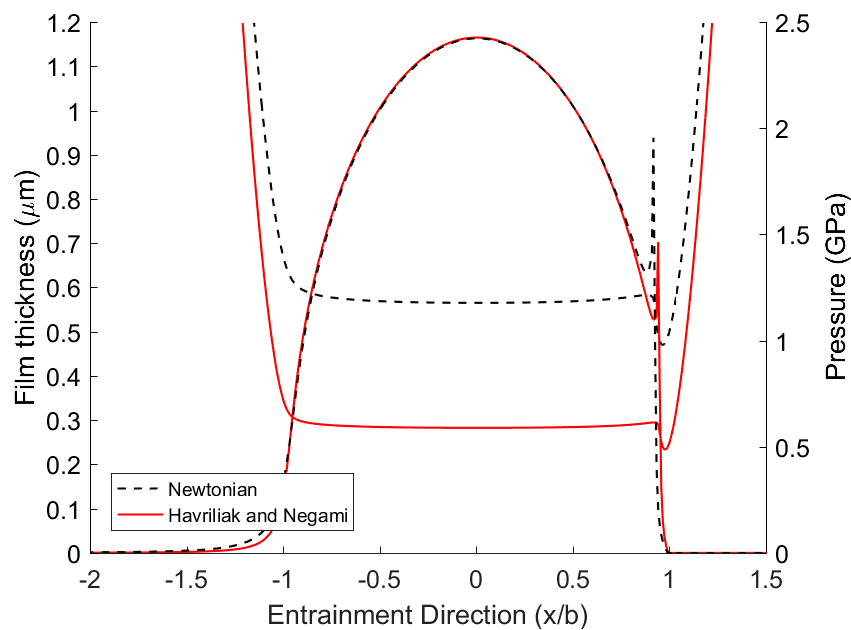


Figure 9. Pressure and film thickness comparison between Newtonian and Havriliak and Negami Non-Newtonian behavior (LLTCA input).

As shown earlier, the contact appears more starved when taking shear thinning into account. This is shown by the reduced pressure spike at the contact exit for the non-Newtonian response, as well as the reduced film thickness.

It is noteworthy that since the gears considered in this study are for a high-performance application, the typical composite surface roughness values are well below $0.1 \mu\text{m}$. For the LLTCA meshing cycle, including lubricant shear thinning, the Stribeck film ratio remains around 6.5. Thus, with the film thickness values encountered in this study, it is evident that the probability of asperity contact is negligible. Therefore, rough surface interactions are neglected in the current analysis.

Figure 10 shows the pressure distribution and the corresponding film thickness throughout a meshing cycle using the LLTCA input to the analysis with non-Newtonian shear taken into account under isothermal conditions. The equivalent Hertzian pressure distribution, which is applicable to dry elastostatic contact conditions, is also included on all the figures. This shows that the pressure distribution closely follows the Hertzian pressure profile except for the inlet hydrodynamic trail and the secondary pressure peak (i.e., the pressure spike or pip) in the vicinity of contact exit. As the inlet trail shrinks toward the edge of the Hertzian domain, contact starvation grows, leading to the diminution of the exit pressure spike. With increased loading and reduced contact kinematics as well as shear thinning, the exit pressure spike tends to the edge of Hertzian region with a reduced magnitude. In the extreme case of starvation, the pressure distribution tends to the Hertzian condition. This trend can be observed in the results of Figure 10, and it has been observed by many authors, including with experimental verification [51–53].

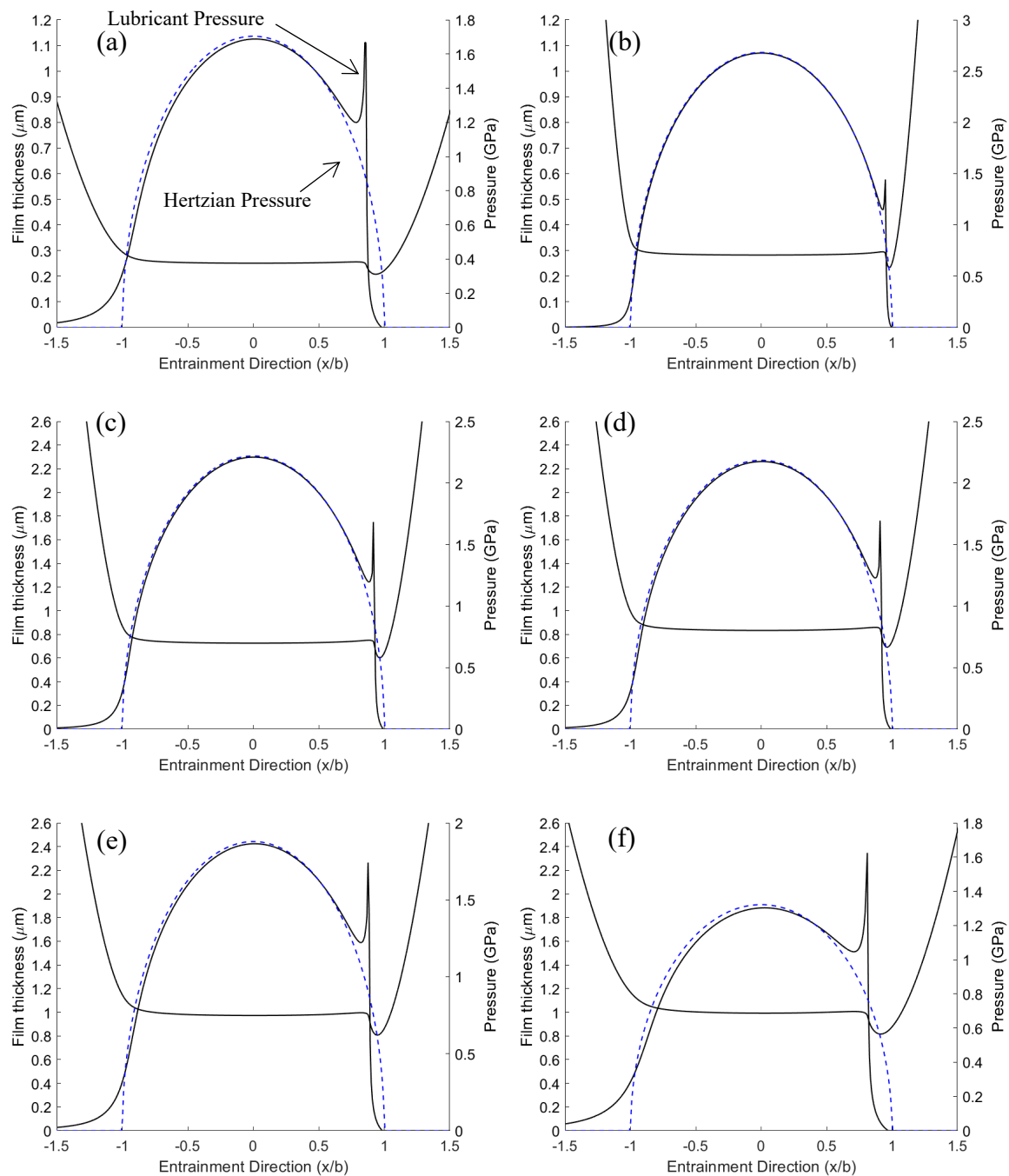


Figure 10. Pressure and film thickness across the contact for mesh point (a) 0.056, (b) 0.25, (c) 0.472, (d) 0.666, (e) 0.917, and (f) 0.972 for the Havriliak and Negami cases.

For high-performance transmissions, it is important to be able to accurately predict the frictional power loss. Due to high lubricant shear strain rates in gear teeth meshing, the shear stress of the lubricant occurs mostly beyond the Eyring shear stress (i.e., non-Newtonian traction). Under these conditions, shear stress is no longer dependent on the lubricant film thickness, but it is dependent on the generated contact pressure. Hence, friction with input from both LLTCA and TCA are quite similar as shown in Figure 11. However, one should note that in practice, as the gear teeth go through numerous meshing cycles, the average temperature of the lubricant would rise as a result. In turn, this would reduce the local viscosity, resulting in an overall reduction in the generated viscous friction.

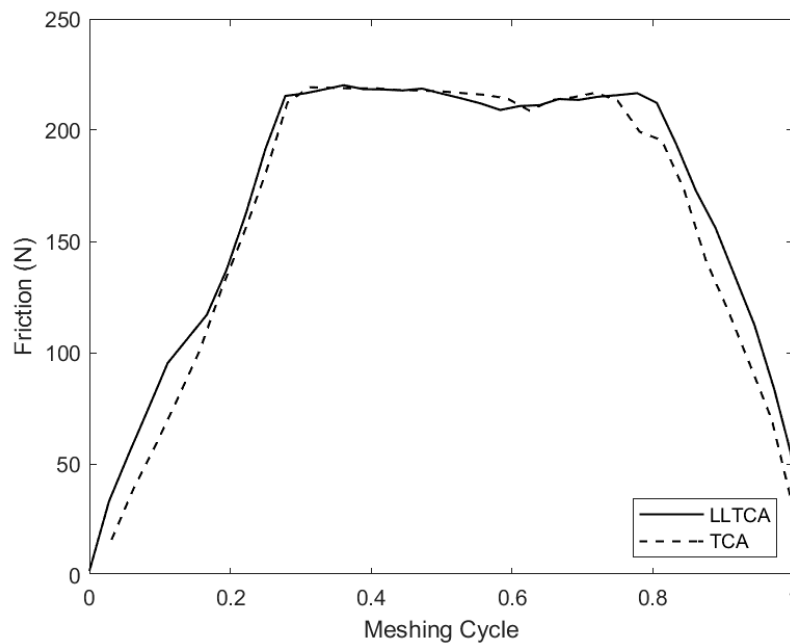


Figure 11. Friction comparison between LLTCA and TCA for a complete meshing cycle.

Figure 12 illustrates the resulting generated contact temperature of the meshing surfaces throughout the meshing cycle with LLTCA input.

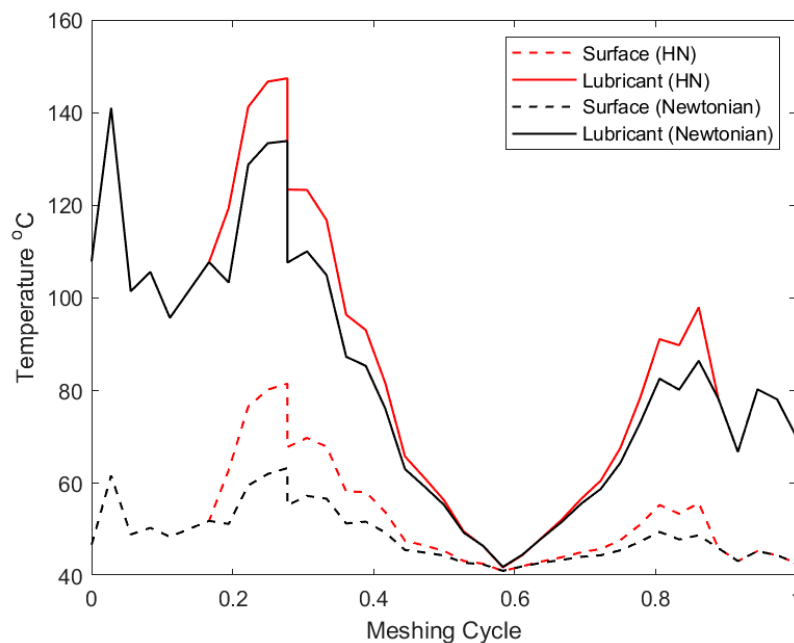


Figure 12. Surface flash temperature of meshing bodies for Newtonian and non-Newtonian conditions for a complete meshing cycle.

Given the assumed initial low bulk lubricant temperature for this analysis, the predicted flash contact temperature is quite reasonable. The greatest contact temperatures occur in regions with highest Deborah number, which is associated with thinnest lubricant film under non-Newtonian traction. With reduced film thickness caused by cases of lubricant shear thinning, the flash temperature of solid surfaces increases accordingly.

Frictional power loss follows the same trend reported in the literature for gearing systems [18,22]. Figure 13 shows that for spur gears, the power loss diminishes at the pitch point, since there is a relative sliding of the meshing gear teeth pair (i.e., pure rolling contact). For both cases of LLTCA and TCA inputs, the power loss is quite similar from the start of meshing to the position of the pitch point. Thereafter, LLTCA input results in greater power loss prediction because of higher predicted sliding velocities. In fact, an increase of 22% is observed at some of the meshing points. Therefore, it is clear that for a more accurate evaluation of transmission efficiency, one should consider measured geometry as in the case of LLTCA. In particular, considering the number of meshing cycles in real applications, such relatively small differences can amount to a large deviation in the prediction of gear efficiency in the long term.

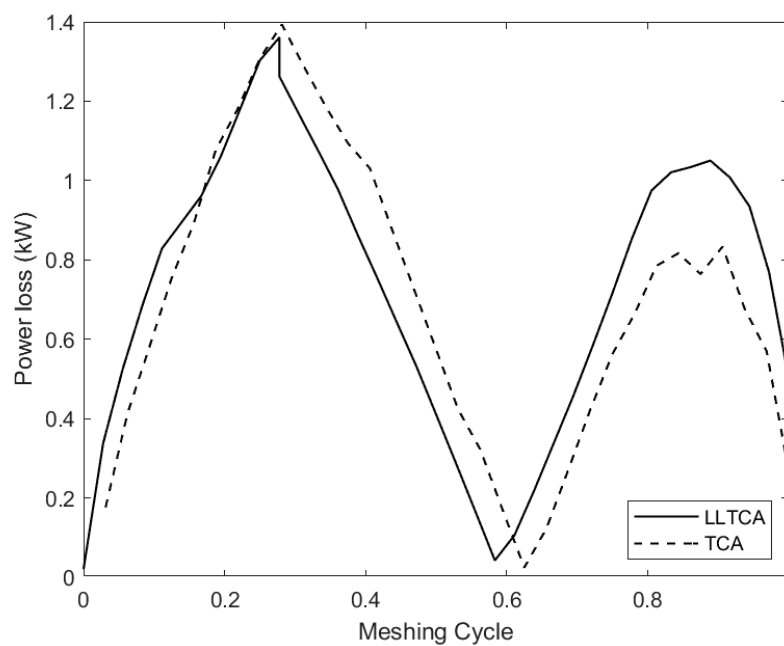
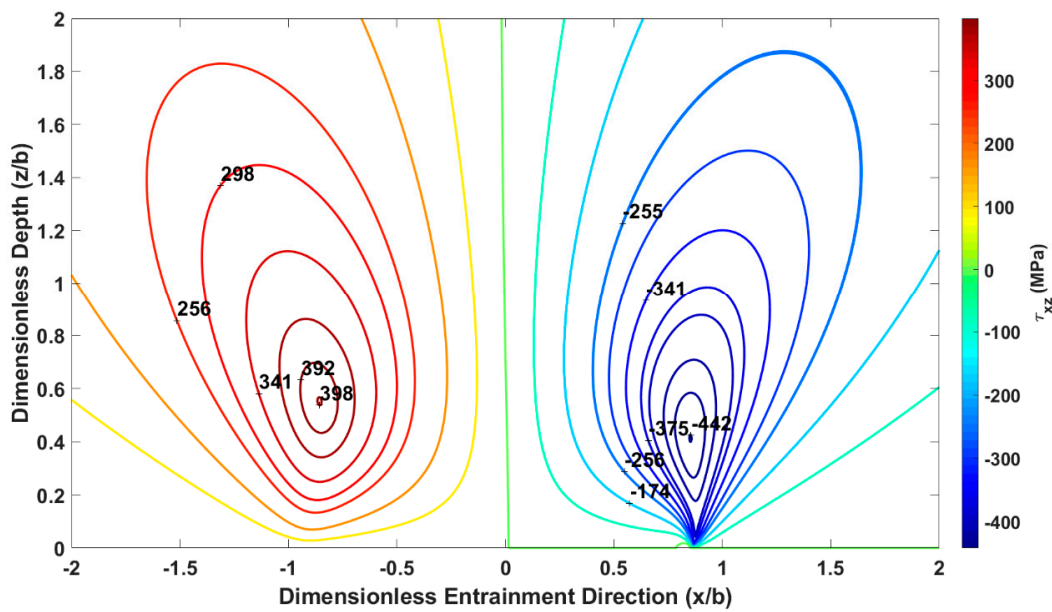


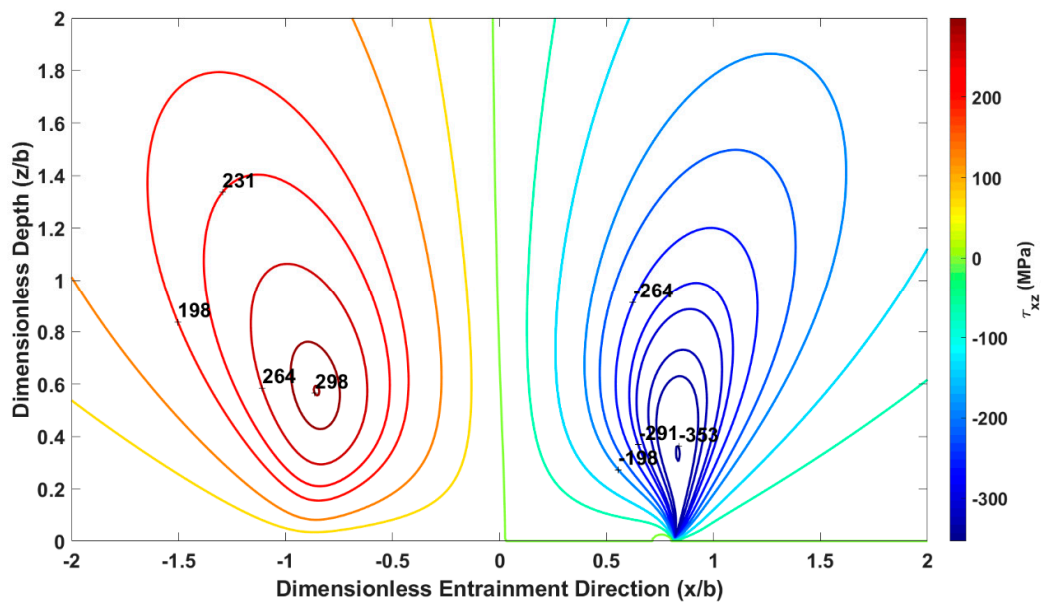
Figure 13. Power loss throughout the meshing cycle.

For high-speed transmissions, which are based mostly on spur and bevel gear pairs, operational reliability is the paramount requirement, as their meshing teeth pairs are subjected to high pressures, shear, and generated temperature. Thin films can result in the direct contact of surfaces and wear. However, one of the main causes of failure is often sub-surface shear stresses of a cyclic nature, potentially causing fatigue spalling [11,49,52]. Figure 14 shows the axisymmetric nature of the orthogonal shearing stresses, τ_{xz} at the beginning and the end of a meshing cycle. The pressure spike in the vicinity of contact exit induces a localized sub-surface field of its own, which is similar to the observations of Paouris et al. [50].

Sub-surface stresses are dependent on the generated contact pressure and friction. Since both LLTCA and TCA predict similar friction, henceforth, the analysis focuses on the difference between Newtonian and non-Newtonian LLTCA cases only.



(a)



(b)

Figure 14. Sub-surface orthogonal shear stress τ_{xz} contours for meshing point (a) 1/18th, and (b) 35/36th position in the meshing cycle.

The equivalent stress with the maximum alternating shear stress hypothesis, which is shown to be the closer representation of fatigue failures of bearings and gears [46,48], is given as:

$$\sigma_e = |\tau_{zxmax} - \tau_{zxmin}| \tag{51}$$

where τ_{zxmax} and τ_{zxmin} are the alternating maximum and minimum shear stresses as in Figure 14a,b. As the equivalent stress approaches the yield of the material, failure due to fatigue spalling can occur in the presence of any sub-surface flaws such as pores or inclusions. Therefore, the larger the value of

equivalent stress, the greater the chance of inelastic deformation due to sub-surface alternating shear stresses. Figure 15 shows that non-Newtonian shear yields higher orthogonal shear stresses.

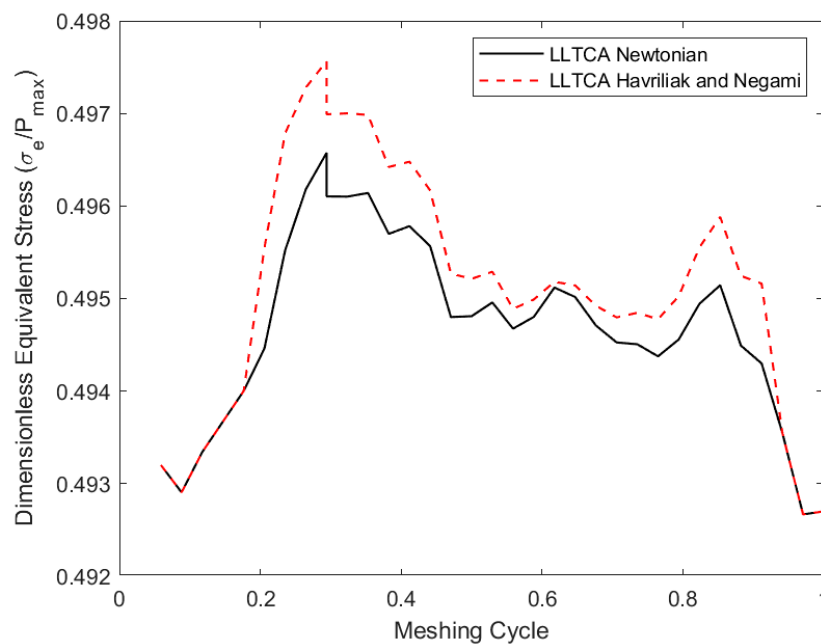


Figure 15. Dimensionless equivalent stress along a complete meshing cycle.

Most gear meshing is subjected to the shear thinning of lubricant and non-Newtonian regime of traction under thermal EHL. Therefore, the prevalent sub-surface stress conditions are best represented by alternating shear stresses under non-Newtonian conditions.

7. Conclusions

The paper provides a comprehensive study of EHL of a meshing spur gear pair. Unlike previous studies reported in the open literature, the contact geometry and contact kinematics are obtained using both Loaded Lubricated Tooth Contact Analysis (LLTCA) instead of the traditional Tooth Contact Analysis (TCA). Therefore, more representative data are used in the subsequent EHL analysis of meshing teeth pairs. Furthermore, the effect of contact temperature rise, as well as the local non-Newtonian shear characteristics of the lubricant, affecting lubricant's rheology, thus film thickness, friction, and power loss have been included in this study. This is more representative of real-life situations for high-performance transmissions, which have not hitherto been reported in the literature. It is shown that the shear thinning of the lubricant due to its non-Newtonian behavior significantly alters the predicted thermal conditions and power loss within the contact. Furthermore, high generated pressures and non-Newtonian traction lead to an increase in the sub-surface equivalent stress, based on the alternating reversing orthogonal shear stresses relative to the usually assumed Newtonian shear. This means that under representative conditions, thermo-EHL with non-Newtonian shear can lead to an increased chance of fatigue spalling throughout a typical meshing cycle. The paper also shows that predicted geometry and contact kinematics using traditional TCA may not be sufficient to accurately predict the friction and durability of spur gear pairs in high-performance applications. Furthermore, the study prompts future investigations into a detailed analysis of gear efficiency and overall performance, based on the LLTCA approach reported here.

Author Contributions: Conceptualization, G.S. and R.R.; methodology, R.R. and H.R.; software, G.S.; validation, G.S.; formal analysis, G.S., R.R., H.R.; investigation, G.S.; data curation, G.S.; writing—original draft preparation, G.S.; writing—review and editing, R.R. and H.R.; visualization, G.S.; supervision, R.R. and H.R.; project administration, H.R.. All authors have read and agreed to the published version of the manuscript.

Funding: The authors would like to express their gratitude for the financial support of the Engineering and Physical Sciences Research Council (EPSRC) extended to this research under the Centre for Doctoral Training for Embedded Intelligence (CDT-EI) and AVL List GmbH, grant reference: EP/L014998/1.

Conflicts of Interest: The authors declare no conflict of interest.

Nomenclature

A_{EHL}	Area of contact
a_v	Vogel viscosity constant
b	Hertzian semi-half-width of the contact
b_v, c_v	Vogel viscosity constants
c_p	Specific heat capacity of the lubricant
c_s	Specific heat capacity of the solids body
D	Deborah number
E'	Equivalent/reduced Young's modulus of elasticity: $\left(2/\left(\frac{1-\nu_1^2}{E_1} + \frac{1-\nu_2^2}{E_2}\right)\right)$
F	Havriliak and Negami non-Newtonian function
f_r	Friction
G_e, G_v	Parameters for the Greenwood chart
G^*	Dimensionless materials' parameter
H_c	Dimensionless film thickness ($H_c = h_c/R'$)
h	Film thickness
h_0	Minimum film thickness for the undeformed (rigid) profile
h_c	Central contact film thickness
i, j	Nodal position identifier
k_l	Thermal conductivity of the lubricant
k_s	Thermal conductivity of the solids
l	Contact length
\dot{m}	Lubricant mass flow rate
n	Iteration counter
p	Pressure
\bar{p}	Average contact pressure ($W/4bl$)
p_{max}	Maximum Hertzian elastic line contact pressure ($\sqrt{WE'/2\pi R'}$)
\dot{Q}	Rate of heat generation
$\dot{Q}_{1,2}$	Heat conducted away through the bounding surfaces
\dot{Q}_{cv}	Heat convected away by the lubricant
q	Shear field
R'	Radius of curvature of equivalent solid
R_i	Conductive thermal resistivity of the lubricant
R_e	Convective thermal resistivity of the lubricant
r_x	Radius of curvature in the direction of entraining motion
r_y	Radius of curvature in the side leakage direction
U	Rolling velocity in the direction of lubricant entrainment ($u_1 + u_2$)
\bar{U}	Speed of entraining motion ($(u_1 + u_2)/2$)
ΔU	Relative sliding velocity ($u_1 - u_2$)
U^*	Dimensionless (rolling) velocity parameter
V	Velocity in the slide leakage direction ($v_1 + v_2$)
W	Applied load
W_p	Load carrying capacity of the lubricant
W^*	Dimensionless load parameter
s	Undeformed geometrical contact profile
x, y	Cartesian coordinate set
T	Bulk temperature
T_0	Atmospheric reference temperature
t	Time

Greek Symbols

α_0	Piezoviscosity coefficient at ambient temperature
$\bar{\alpha}$	Piezoviscosity coefficient at specified temperature
α_{HN}, β_{HN}	Havriliak and Negami parameters
$\dot{\gamma}$	Shear rate
δ	Localized elastic deflection
ζ	Evans and Johnson's friction parameter
η_0	Viscosity at rest temperature and atmospheric pressure
η	Dynamic viscosity of the lubricant
η_c	Dynamic viscosity at the center of the contact
η_p	Piezoviscosity of the lubricant (solely dependent on pressure)
θ_0	Bulk flow temperature
$\Delta\theta$	Temperature rise
λ	Relaxation time
μ	Coefficient of friction
ρ	Density of the lubricant
ρ_c	Density at the center of the contact
ρ'	Density of the solid bodies
ς	Load relaxation parameter
σ_e	Equivalent stress
τ	Shear stress
τ_l	Limiting shear stress
τ_0	Characteristic shear stress
Ω	Pressure relaxation parameter
χ_i	Thermal partitioning coefficient

Abbreviations

1D	One-Dimensional
CMM	Coordinate Measuring Machine
EHL	Elastohydrodynamic Lubrication
EIN	Effective Influence Newton–Raphson
FEA	Finite Element Analysis
HN	Havriliak–Negami
LLTCA	Lubricated Loaded Tooth Contact Analysis
NVH	Noise, Vibration, and Harshness
TCA	Tooth Contact Analysis

Appendix A

The gear parameters and assembly used for this investigation are shown below; further details are found in Oglieve et al. [19].

Table A1. Gear pair specification [19].

Gear Type	Spur
Pinion No. Teeth	13
Wheel No. Teeth	35
Gear Module	3.8
Center Distance	90 mm
Gear Width	13.3 mm

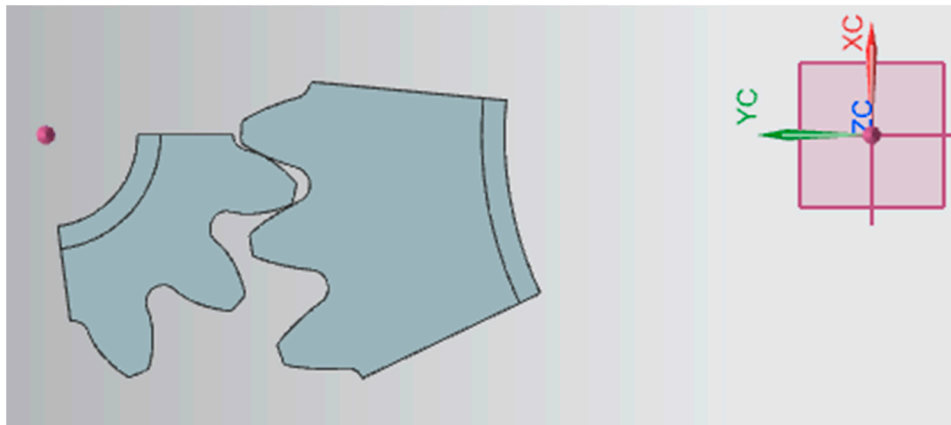


Figure A1. Gear geometry assembly [19].

References

1. Mohammadpour, M.; Theodossiades, S.; Rahnejat, H.; Kelly, P. Transmission efficiency and noise, vibration and harshness refinement of differential hypoid gear pairs. *J. Multi-Body Dynamics* **2014**, *228*, 19–33. [\[CrossRef\]](#)
2. Wu, S.; Cheng, H.S. A Friction Model of Partial-EHL Contacts and its Application to Power Loss in Spur Gears. *Tribol. Trans.* **1991**, *34*, 398–407. [\[CrossRef\]](#)
3. Diab, Y.; Ville, F.; Velex, P. Investigations on power losses in high-speed gears. *J. Eng. Tribol.* **2006**, *220*, 191–198. [\[CrossRef\]](#)
4. Li, S.; Kahraman, A. Prediction of Spur Gear Mechanical Power Losses Using a Transient Elastohydrodynamic Lubrication Model. *Tribol. Trans.* **2010**, *53*, 554–563. [\[CrossRef\]](#)
5. Petry-Johnson, T.T.; Kahraman, A.; Anderson, N.E.; Chase, D.R. An Experimental Investigation of Spur Gear Efficiency. *J. Mech. Des.* **2008**, *130*, 062601. [\[CrossRef\]](#)
6. Li, S.; Kahraman, A. A tribo-dynamic model of a spur gear pair. *J. Sound Vib.* **2013**, *332*, 4963–4978. [\[CrossRef\]](#)
7. Velex, P.; Maatar, M. A mathematical model for analyzing the influence of shape deviations and mounting errors on gear dynamic behaviour. *J. Sound Vib.* **1996**, *191*, 629–660. [\[CrossRef\]](#)
8. Kahraman, A.; Blankenship, G.W. Effect of Involute Tip Relief on Dynamic Response of Spur Gear Pairs. *J. Mech. Des.* **1999**, *121*, 313–315. [\[CrossRef\]](#)
9. Parker, R.; Vijayakar, S.; Imajo, T. Non-linear dynamic response of a spur gear pair: Modelling and experimental comparisons. *J. Sound Vib.* **2000**, *237*, 435–455. [\[CrossRef\]](#)
10. Cooley, C.G.; Liu, C.; Dai, X.; Parker, R.G. Gear tooth mesh stiffness: A comparison of calculation approaches. *Mech. Mach. Theory* **2016**, *105*, 540–553. [\[CrossRef\]](#)
11. Johns-Rahnejat, P.M.; Gohar, R. Point contact elastohydrodynamic pressure distribution and sub-surface stress field. In *Int. Tri-Annual Conf. on Multi-Body Dynamics: Monitoring and Simulation Techniques*; Bradford: Yorkshire, UK, 1997; pp. 161–177.
12. Ding, Y.; Rieger, N.F. Spalling formation mechanism for gears. *Wear* **2003**, *254*, 1307–1317. [\[CrossRef\]](#)
13. Tao, J.; Hughes, T.G.; Evans, H.P.; Snidle, R.W.; Hopkinson, N.A.; Talks, M.; Starbuck, J.M. Elastohydrodynamic Lubrication Analysis of Gear Tooth Surfaces from Micropitting Tests. *J. Tribol.* **2003**, *125*, 267–274. [\[CrossRef\]](#)
14. Moss, J.; Kahraman, A.; Wink, C. An Experimental Study of Influence of Lubrication Methods on Efficiency and Contact Fatigue Life of Spur Gears. *J. Tribol.* **2018**, *140*, 051103. [\[CrossRef\]](#)
15. Litvin, F.L.; Fuentes, A. *Gear Geometry and Applied Theory*; Cambridge University Press (CUP): Cambridge, UK, 2004.
16. Vijayakar, S.M. *Tooth Contact Analysis Software: CALYX*; Advanced Numerical Solutions: Hilliard, OH, USA, 1998.
17. Karagiannis, I.; Theodossiades, S.; Rahnejat, H. On the dynamics of lubricated hypoid gears. *Mech. Mach. Theory* **2012**, *48*, 94–120. [\[CrossRef\]](#)
18. Fatourehchi, E.; Elisaus, V.; Mohammadpour, M.; Theodossiades, S.; Rahnejat, H. Efficiency and Durability Predictions of High Performance Racing Transmissions. *SAE Int. J. Passeng. Cars Mech. Syst.* **2016**, *9*, 1117–1124. [\[CrossRef\]](#)

19. Oglieve, C.; Sivayogan, G.; Mohammadpour, M.; Rahnejat, H. Lubricated loaded tooth contact analysis for spur gear pair. *Int. J. Powertrains* **2019**, *8*, 23–39. [[CrossRef](#)]
20. Radzevich, S.P.; Dudley, D.W. *Handbook of Practical Gear Design*; CRC Press: Boca Raton, FL, USA, 1994.
21. And, P.S.; Velez, P.; Duverger, O.; Sainsot, P. Contribution of Gear Body to Tooth Deflections—A New Bidimensional Analytical Formula. *J. Mech. Des.* **2004**, *126*, 748–752.
22. Elisaus, V.; Mohammadpour, M.; Theodossiades, S.; Rahnejat, H. Effect of teeth micro-geometrical form modification on contact kinematics and efficiency of high performance transmissions. *J. Multi-body Dyn.* **2017**, *231*, 538–555. [[CrossRef](#)]
23. Litvin, F.L.; Fuentes, A.; Hayasaka, K. Design, manufacture, stress analysis, and experimental tests of low-noise high endurance spiral bevel gears. *Mech. Mach. Theory* **2006**, *41*, 83–118. [[CrossRef](#)]
24. Evans, C.R.; Johnson, K.L. Regimes of Traction in Elastohydrodynamic Lubrication. *J. Mech. Eng. Sci.* **1986**, *200*, 313–324. [[CrossRef](#)]
25. Chittenden, R.J.; Dowson, D.; Dunn, J.F.; Taylor, C.M. A theoretical analysis of the isothermal elastohydrodynamic lubrication of concentrated contacts. I. Direction of lubricant entrainment coincident with the major axis of the Hertzian contact ellipse. *Proc. R. Soc. London Ser. A. Math. Phys. Sci.* **1985**, *397*, 245–269.
26. Olver, A.V. Gear lubrication—A review. *J. Eng. Tribol.* **2002**, *216*, 255–267. [[CrossRef](#)]
27. Gohar, R. *Elastohydrodynamics*; World Scientific Pub Co Pte Lt: Singapore, Singapore, 2001.
28. Hamrock, B.J.; Jacobson, B.O. Elastohydrodynamic Lubrication of Line Contacts. *ASLE Trans.* **1984**, *27*, 275–287. [[CrossRef](#)]
29. Paouris, L.; Rahmani, R.; Theodossiades, S.; Rahnejat, H.; Hunt, G.; Barton, W. An Analytical Approach for Prediction of Elastohydrodynamic Friction with Inlet Shear Heating and Starvation. *Tribol. Lett.* **2016**, *64*, 10. [[CrossRef](#)]
30. Havriliak, S.; Negami, S. A complex plane representation of dielectric and mechanical relaxation processes in some polymers. *Polymer* **1967**, *8*, 161–210. [[CrossRef](#)]
31. Houpert, L. New Results of Traction Force Calculations in Elastohydrodynamic Contacts. *J. Tribol.* **1985**, *107*, 241–245. [[CrossRef](#)]
32. Vogel, H. The temperature dependence law of the viscosity of fluids. *Phys. Z.* **1921**, *22*, 645–646.
33. Crouch, R.F.; Cameron, A. Viscosity-temperature equations for lubricants. *J. Inst. Pet* **1961**, *47*, 307–313.
34. Gohar, R.; Rahnejat, H. *Fundamentals of Tribology*; World Scientific Pub Co Pte Lt: Singapore, Singapore, 2008.
35. Yang, P.; Cui, J.; Jin, Z.M.; Dowson, D. Transient elastohydrodynamic analysis of elliptical contacts. Part 2: Thermal and Newtonian lubricant solution. *J. Eng. Tribol.* **2005**, *219*, 187–200. [[CrossRef](#)]
36. Greenwood, J.A. Presentation of Elastohydrodynamic Film-Thickness Results. *J. Mech. Eng. Sci.* **1969**, *11*, 128–132. [[CrossRef](#)]
37. Reiner, M. The Deborah Number. *Phys. Today* **1964**, *17*, 62. [[CrossRef](#)]
38. Bezot, P.; Hesse-Bezot, C.; Dalmaz, G.; Taravel, P.; Vergne, P.; Berthe, D. A study of traction in elastohydrodynamic lubrication: Experimental and simulated curves for a point contact lubricated by a silicone fluid. *Wear* **1988**, *123*, 13–31. [[CrossRef](#)]
39. Morris, N.; Rahmani, R.; Rahnejat, H.; King, P.; Fitzsimons, B. Tribology of piston compression ring conjunction under transient thermal mixed regime of lubrication. *Tribol. Int.* **2013**, *59*, 248–258. [[CrossRef](#)]
40. Paouris, L.; Rahmani, R.; Theodossiades, S.; Rahnejat, H.; Hunt, G.; Barton, W. Inefficiency predictions in a hypoid gear pair through tribodynamics analysis. *Tribol. Int.* **2018**, *119*, 631–644. [[CrossRef](#)]
41. Olver, A.V.; Spikes, H.A. Prediction of traction in elastohydrodynamic lubrication. *J. Eng. Tribol.* **1998**, *212*, 321–332. [[CrossRef](#)]
42. Sharif, K.J.; Evans, H.P.; Snidle, R.W.; Newall, J.P. Modeling of Film Thickness and Traction in a Variable Ratio Traction Drive Rig. *J. Tribol.* **2004**, *126*, 92–104. [[CrossRef](#)]
43. Jalali-Vahid, D.; Gohar, R.; Rahnejat, H.; Jin, Z.M. Prediction of oil-film thickness and shape in elliptical point contacts under combined rolling and sliding motion. *J. Eng. Tribol.* **2000**, *214*, 427–437. [[CrossRef](#)]
44. Eyring, H. Viscosity, Plasticity, and Diffusion as Examples of Absolute Reaction Rates. *J. Chem. Phys.* **1936**, *4*, 283. [[CrossRef](#)]
45. Hoglund, E.; Jacobson, B. Experimental Investigation of the Shear Strength of Lubricants Subjected to High Pressure and Temperature. *J. Tribol.* **1986**, *108*, 571–577. [[CrossRef](#)]

46. Rahnejat, H.; Johns-Rahnejat, P.M. Mechanics of Contacting Surfaces. In *Encyclopedia of Automotive Engineering*; John Wiley and Sons: Hoboken, NJ, USA, 2014.
47. Johnson, K.L. *Contact Mechanics*; Cambridge University Press (CUP): Cambridge, UK, 1985.
48. Ioannides, E.; Harris, T.A. A New Fatigue Life Model for Rolling Bearings. *J. Tribol.* **1985**, *107*, 367–377. [[CrossRef](#)]
49. Rahnejat, H.; Rahmani, R.; Mohammadpour, M.; Johns-Rahnejat, P.M. Tribology of power train systems. *ASM Handb.* **2017**, *18*, 916–934.
50. Paouris, L.; Theodossiades, S.; De la Cruz, M.; Rahnejat, H.; Kidson, A.; Hunt, G.; Barton, W. Lubrication analysis and sub-surface stress field of an automotive differential hypoid gear pair under dynamic loading. *J. Mech. Eng. Sci.* **2016**, *230*, 1183–1197. [[CrossRef](#)]
51. Hamilton, G.M.; Moore, S.L. Deformation and pressure in an elastohydrodynamic contact. *Proc. R. Soc. London Ser. A. Math. Phys. Sci.* **1971**, *322*, 313–330.
52. Johns-Rahnejat, P.M. Pressure and Stress Distribution under Elastohydrodynamic Point Contacts. Ph.D. Thesis, Imperial College, University of London, London, UK, 1988.
53. Jalali-Vahid, D.; Rahnejat, H.; Gohar, R.; Jin, Z.M. Comparison between experiments and numerical solutions for isothermal elastohydrodynamic point contacts. *Appl. Phys.* **1998**, *31*, 2725–2732. [[CrossRef](#)]



© 2020 by the authors. Licensee MDPI, Basel, Switzerland. This article is an open access article distributed under the terms and conditions of the Creative Commons Attribution (CC BY) license (<http://creativecommons.org/licenses/by/4.0/>).